High-pressure behavior of 3.65 Å phase: Insights from Raman spectroscopy

ABHISEK BASU^{1,*}, MAINAK MOOKHERJEE^{1,†}, CHRISTELLE BUCAG¹, SERGEY TKACHEV², AND BERND WUNDER³

¹Earth Materials Laboratory, Earth, Ocean and Atmospheric Science, Florida State University, Tallahassee, Florida 32306, U.S.A.

²Center for Advanced Radiation Sources, University of Chicago, Chicago, Illinois 60637, U.S.A.

³Deutsches GeoForschungsZentrum GFZ, Section 3.6, Telegrafenberg, 14473 Potsdam, Germany

ABSTRACT

The 3.65 Å phase [MgSi(OH)₆] is a hydrous phase that is predicted to be stable in a simplified MgO-SiO₂-H₂O (MSH) ternary system at pressures exceeding 9 GPa. Along cold subduction zones, it is likely to transport water, bound in its crystalline lattice, into the Earth's interior. The 3.65 Å phase consists of Mg and Si octahedral sites attached to the hydroxyl group that forms a hydrogen bond and is predicted to undergo pressure-induced symmetrization of the hydrogen bond. Therefore, in this study, we investigate the high-pressure behavior of the 3.65 Å phase using Raman spectroscopy. We have conducted five distinct compressions up to ~60 GPa using two different pressure-transmitting media—alcohol mixture and neon. At ambient conditions, we identified vibrational modes using complementary first-principles simulations based on density functional perturbation theory. Upon compression, we note that the first derivative of the vibrational modes in the lattice region stiffens, i.e., $b_i^{\text{lattice}} > 0$. In contrast, the hydroxyl region softens, i.e., $b_i^{\text{OH}} > 0$. This is indicative of the strengthening of hydrogen bonding upon compression. We noticed a significant broadening of vibrational modes related to hydroxyl groups that are indicative of proton disorder. However, within the maximum pressures explored in this study, we did not find evidence for pressure-induced symmetrization of the hydrogen bonds. We used the pressure derivative of the vibrational modes to determine the ratio of the bulk moduli and their pressure derivative. We note that the smaller bulk moduli of hydrous phases compared to the major mantle phases are compensated by significantly larger pressure derivatives of the bulk moduli for the hydrous phases. This leads to a significant reduction in the elasticity contrast between hydrous and major mantle phases. Consequently, the detection of the degree of mantle hydration is likely to be challenging at greater depths.

Keywords: Subduction zone, hydrous mineral phases, 3.65 Å phase, high-pressure Raman spectroscopy, diamond-anvil cell (DAC), hydrogen bonding

Introduction

Water exerts a significant influence on the dynamics of the solid Earth. For instance, water is known to lower melting temperatures (Hirschmann 2006) and affects transport properties including the rheology of the mantle (Karato 2010). Thus, considerable research has been done to understand how water is transported into the deep Earth and how much water is stored in the deep Earth. The efficiency of the transport of water is related to the thermodynamic stability of mineral phases including hydrous minerals and nominally anhydrous minerals. It is well known that hydrous phases often have limited thermal stabilities and hence they tend to dehydrate releasing water. The released aqueous fluids affect the surrounding mantle, which eventually leads to the melting of the overlying mantle wedge and is known to trigger earthquakes (Iwamori 1998, 2004, 2007; Kawamoto 2006). However, a part of the water is retained in dense hydrous phases which are efficient in transporting water to greater depths. Hence, significant research has been conducted to quantify the

phase stabilities of hydrous phases (Kawamoto 2006; Pawley et al. 2011). Recent experimental studies on the simplified ternary system for hydrated mantle lithosphere, i.e., the MgO-SiO₂-H₂O (MSH) system have documented the existence of 3.65 Å phase—a thermodynamically stable form of MgSi(OH)₆ with a structure characterized by lattice plane spacing of 3.65 Å (Wunder et al. 2011, 2012; Koch-Müller et al. 2021) at pressures of 9–10 GPa. This phase is formed from the breakdown of the 10 Å phase [Mg₃Si₄O₁₀(OH)₂.·*n*H₂O] (Pawley et al. 2011; Wunder et al. 2011, 2012; Koch-Müller et al. 2021). The 3.65 Å phase could potentially transport ~35 wt% water, bound in its crystalline lattice, into the deep interior.

How much water is efficiently transported and sequestered in the deep Earth can be better understood if we can map the degree of mantle hydration. Thus it is crucial to have better constraints on the elastic and transport properties of these hydrous phases and nominally anhydrous phases and relate these constraints on the physical properties of the mineral aggregates with the geophysical observables. A key issue is that these hydrous phases often have high compressibility than that of nominally anhydrous phases, and it is quite important to have a better understanding

^{*} E-mail: abasu@fsu.edu Orcid 0000-0002-0283-1778

[†] Orcid 0000-0002-0605-5964

of how pressure and temperature affect the atomistic structure and which in turn influences the physical properties of these minerals. Most of the hydrous phases are characterized by hydrogen bonding, which, upon compression may evolve to a pressure-induced symmetrization. This often leads to significant changes in physical properties including elasticity such that the properties of hydrous phases could become indistinguishable from that of the bulk of the mantle, i.e., nominally anhydrous phases (Tsuchiya et al. 2002, 2005).

Recent first-principles simulations on the 3.65 Å phase have predicted the hydroxyl (OH) bond length (d_{OH}) to increase and the corresponding $(d_{0\cdots 0})$ distance to shorten considerably under compression eventually resulting in a hydrogen bondsymmetrization at pressures ~60 GPa (Mookherjee et al. 2015). Hydrogen-bond symmetrization occurs when the hydrogen atom in an (O-H···O) unit is located exactly at the center of the $(d_{O\cdots O})$ unit, i.e., $(d_{OH} = \frac{1}{2}d_{O\cdots O})$. Several, hydrogen-bearing mineral phases have been predicted to undergo similar hydrogen-bond symmetrization including δ-AlOOH, β-CrOOH, phase-D, phase-H, and phase-Egg. For instance, δ-AlOOH undergoes symmetrization at ~16-24 GPa (Panero and Stixrude 2004; Sano-Furukawa et al. 2008), β-CrOOH at ~5 GPa (Jahn et al. 2012), and Phase-D at ~40 GPa (Tsuchiya et al. 2002). However, many of these studies are based on theoretical predictions and the predicted symmetrization pressures often differ from the experimental observations. For instance, a vibrational spectroscopic study on phase-D indicated the symmetrization to occur at a higher pressure (Shieh et al. 2009). So, it is important to test the theoretical predictions through high-pressure experiments.

In this study, we explore the high-pressure behavior of the 3.65 Å phase using Raman spectroscopy with particular emphasis on the evolution of the hydroxyl stretching to understand pressure-induced changes in hydrogen bonding. In addition, we also explore the pressure evolution of the low-wavenumber modes to provide a better constraint on the ratio of bulk modulus and its pressure derivative.

METHODS

The sample of 3.65 Å phase studied was synthesized at 10 GPa and 425 °C (Wunder et al. 2011). The peak pressure and temperature were held for 77 hours in a multi-anvil apparatus at GeoForschungsZentrum, Potsdam, Germany. The synthesized material was characterized using electron microprobe analysis to confirm the stoichiometry of the 3.65 Å phase as MgSi(OH)₆. Powder X-ray diffraction confirmed the structure of the synthesized 3.65 Å phase. The details of the synthesis and the characterization have been reported in earlier studies (Wunder et al. 2011, 2012).

In this study, we explored the high-pressure behavior of the 3.65 Å phase using Raman spectroscopy. The Raman spectra were acquired in a Horiba Jobin Yvon LabRam Evolution spectrometer at the Earth Materials Laboratory, Florida State University. The spectrometer has a backscattering configuration and is equipped with a grating of 1800 lines/mm with a resolution of \sim 2 cm⁻¹. The spectrometer is also equipped with a thermoelectrically cooled CCD detector, an Olympus 50× long working distance infinity-corrected objective. We employed a frequency-doubled Nd-YAG laser (λ = 532 nm) with a 300 mW maximum output power at the source.

It is well known that hydrous mineral phases often have limited thermal stability and are likely to be sensitive to the power of the laser. In a recent study, an incremental increase of laser power resulted in incremental heating of the hydrous mineral sample within the diamond-anvil cell (Basu and Mookherjee 2021). Thus, we explored the effect of laser power on the 3.65 Å phase by increasing the laser power in incremental steps of 10, 25, 50, and 100% (of 300 mW at the source) and collected Raman spectra at ambient conditions. We repeated the stepwise increase of laser power to evaluate the effect of laser power on the sample within

the diamond-anvil cell with the cell closed by its weight, i.e., without any static compression. Upon incrementally increasing the laser power, for the 3.65 Å, we did not observe any identifiable changes in the mode frequency position of the hydroxyl stretching region, $2800-3500~\rm cm^{-1}$ (Online Materials¹ Fig. OM1). However, we optimized the laser power and exposure time to minimize the possibility of damaging the sample from over-exposure and local laser heating. To obtain a good signal-to-noise ratio we acquired Raman spectra of the 3.65 Å phase in the spectral range $100-1250~\rm cm^{-1}$ with an acquisition time of 60 s and 10 accumulations and in the range $2850-3600~\rm cm^{-1}$ with an acquisition time of 30 s and 10 accumulations.

We compressed powdered 3.65 Å phase to high pressures in a symmetric diamond-anvil cell (DAC). The DAC was fitted with two low-fluorescence type Ia diamond anvils. Each anvil had 300 μm diameter culets. We used a stainlesssteel foil of 150 μm thickness as the gasket material. We pre-indented the foil to $50~\mu m$ thickness. A sample chamber hole of $100~\mu m$ diameter was drilled using a Boehler-Almax micro-driller. We conducted five separate static compressions to high pressures. Initially, we conducted two static compressions up to ~20 GPa with an alcohol mixture (methanol:ethanol) as the pressure-transmitting medium (PTM). The hydrostatic limit of alcohol mixture is ~10 GPa (Klotz et al. 2009). This was followed by two static compressions up to ~20 GPa with neon (Ne) gas as the PTM. In addition, we also conducted one static compression up to ~60 GPa with Ne as the PTM. The Ne loading was done at the COMPRES facility, GSECARS, Advanced Photon Source, Argonne National Laboratory (Online Materials¹ Table OM1). Ne is reported to be hydrostatic up to ~15 GPa (Klotz et al. 2009). However, the pressure gradient due to non-hydrostaticity is negligible and the PTM remains quasi-hydrostatic to very high pressures (Fei et al. 2007; Klotz et al. 2009). We compressed the sample to pressures beyond the hydrostatic limit of the alcohol mixture, ~10 GPa (Klotz et al. 2009). This enables us to get insight into the comparative difference between the two PTM i.e., alcohol mixture and Ne gas. We used ruby fluorescence for determining the pressure within the symmetric DAC (Mao et al. 1986).

We have supplemented our Raman experiments with first-principles simulations based on the density functional theory (DFT) (Hohenberg and Kohn 1964; Kohn and Sham 1965). We employed a widely used approximation to the exchangecorrelation functional: the generalized gradient approximation (GGA) (Perdew and Yue 1986; Perdew 1991; Perdew et al. 1996). We have used the highly accurate projector augmented wave method (PAW) (Kresse and Joubert 1999) as implemented in the Vienna ab initio simulation package (VASP) (Kresse and Hafner 1993; Kresse and Furthmüller 1996a, 1996b; Kresse and Joubert 1999). We used the crystal structure of 3.65 Å phase refined at the ambient condition from prior studies (Wunder et al. 2011; Welch and Wunder 2012) as a starting guess for the first-principles simulations. We performed a static first-principles simulation on the primitive unit cell of 3.65 Å phase with a P21 space group with 28 atoms in the unit cell. We used an energy cut-off $E_{cut} = 800$ eV and a Monkhorst-Pack (Monkhorst and Pack 1976) 4 × 4 × 3 k-point mesh, yielding 21 k-points in the irreducible wedge of the Brillouin zone. A series of convergence tests demonstrated that these computational parameters yield total energies that are converged within 5 meV/atom. In contrast to a recent study that focused on the determination of the equation of state using energy vs. volume relationship and pressure dependence of elasticity (Mookherjee et al. 2015), in this study, our goal is to predict vibrational modes under ambient conditions. Hence, for calculating vibrational modes, we used a python based pre- and post-processing code PHONOPY (Togo and Tanaka 2015) in conjunction with the DFT code VASP. We used an experimentally determined zero pressure unit cell volume of 194.52 Å3 and created a 2 × 2 × 2 supercell with 224 atoms and determined the vibrational modes.

RESULTS

The Raman spectra of the 3.65 Å phase are better understood in terms of its crystal structure that has a $P2_1$ space group symmetry. The crystal structure of the 3.65 Å phase consists of alternating MgO₆ and SiO₆ octahedral units that are corner shared. In addition, the hydrogen atoms are bonded to the O atoms to form chains of the hydrogen-bonded network (Fig. 1) (Wunder et al. 2011; Kleppe et al. 2012; Welch and Wunder 2012; Mookherjee et al. 2015). The unit cell of the 3.65 Å phase consists of two formula units (Z = 2) i.e., 28 total atoms (Fig. 1). With three degrees of freedom, the total expected vibrational modes are 84 (42A + 42B). However, three of these modes are

acoustic modes (1A+2B). Thus the total number of optic modes is 81 (41A + 40B) and all these 81 modes are Raman active. The ambient Raman spectra in the lattice region (180-1200 cm⁻¹) and hydroxyl region (2850–3600 cm⁻¹) are compared with the theoretically predicted Raman spectra. Overall the experimentally observed modes are in good agreement with the predicted modes (Fig. 2). However, in the hydroxyl region, the theoretical predictions are slightly lower in energies compared to the experimental results. This was also observed in a recent comparison between experimental and theoretical predictions (Borodina et al. 2020). The experimentally observed Raman spectra show a total of 22 modes in the lattice region and six modes in the hydroxyl region i.e., 28 vibrational modes are observed instead of the expected 81 modes. These could be attributed to low-scattering cross sections of several of the predicted modes which are often not detectable. In addition, several of the predicted modes have vibrational energies that are often too close to be resolved in experimental observations. In agreement with the recent study, the 3.65 Å phase's low-energy region is characterized by MgO₆ and SiO₆ octahedral deformation coupled with translation and libration modes, octahedral stretching or breathing modes, deformation or bending modes associated with the OH, and bending mode associated with the bridging Mg-O-Si units (Borodina et al. 2020) (Fig. 2). In the energy region between 100 and 300 cm⁻¹, we observe several vibrational modes including intense modes at ~194, 262, 268, and 285 cm⁻¹. The vibrational mode at 262 cm⁻¹ is likely due to the libration of the SiO₆ octahedra. The vibrational mode at 268 cm⁻¹ is very likely caused by the deformation motion of the corner shared protonated MgO₆ and SiO₆ octahedral units. The vibrational mode at 285 cm⁻¹ can be attributed to the (Si,Mg)O₆ octahedral deformation and (Mg,O) translational motion (Online Materials1 Fig. OM2; Table 1). In the energy region between 400 and 1000 cm⁻¹, we observe an intense vibrational mode at ~681 cm⁻¹, which is likely to be related to deformational or collective bending of the OH modes primarily associated with the H1 and H2 protons. This is also coupled with motions related to the Si-O-Mg bridging. In the energy region <1000 cm⁻¹, we observe two weaker modes at 1140 and 1176 cm⁻¹ that are likely due to the OH bending motion.

FIGURE 2. Ambient Raman spectra of the 3.65 Å phase in the low wavenumber and hydroxyl stretching region. The theoretically predicted modes A and B are shown as blue and red dash, respectively. The eigenvectors of the atomic vibrations for selective modes are indicated in the inset. (Color online.)

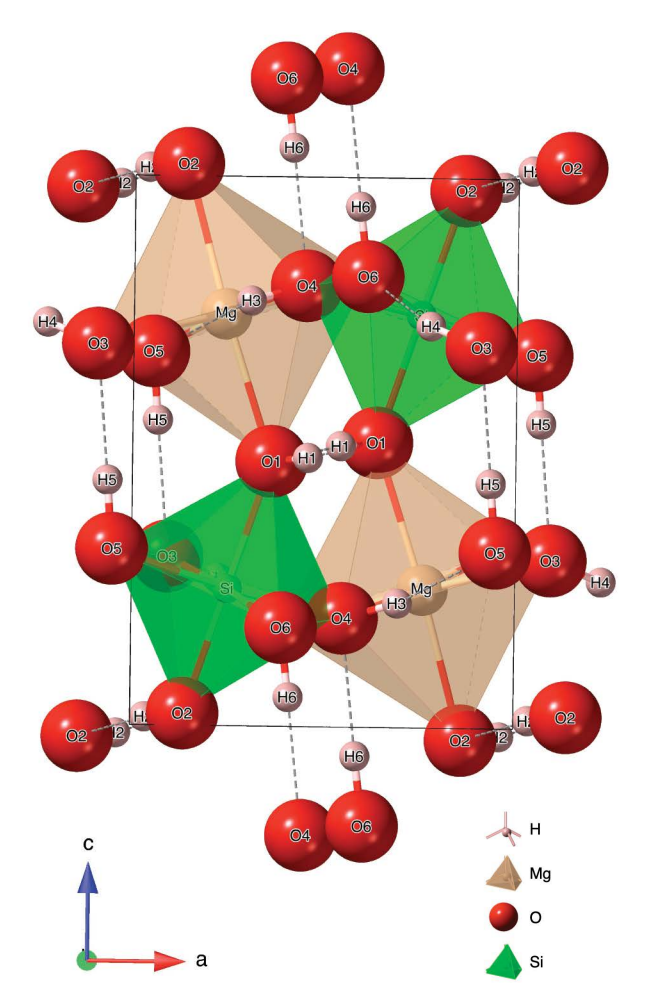


FIGURE 1. Crystal structure of 3.65 Å phase projected down *b*-axis, i.e., showing the *a-c* plane. The crystal structure of the 3.65 Å phase consists of alternating Mg- (beige) and Si- (light green) octahedral units that share corners. All the corner O atoms (red) are attached to H atoms (pink), which form six distinct pairs of hydrogen bonding (dashed lines). (Color online.)

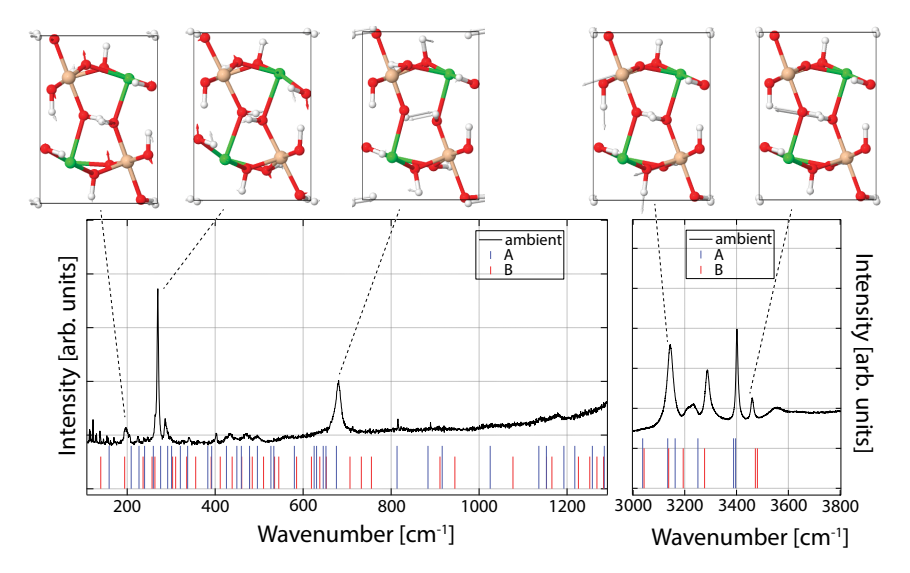


TABLE 1. Low-wavenumber Raman mode assignments

-		3.65 Å
	This study	Borodina et al. (2020)
Mode assignment ^a	ν (cm ⁻¹)	ν (cm ⁻¹)
	156 w	
(Si,Mg)O ₆ rot. + (Si,Mg) tr.	194 w	197
	205 w	
	224 w	
	238 w	
	245 w	
SiO ₆ rot.	262 s	265
(Si,Mg)O ₆ def. + Mg tr.	268 vs	271
$(Si,Mg)O_6$ def. + (Mg,O) tr.	285 s	290
		300
	325 w	
	340 w	
SiO ₆ sym. stretch+(Si,Mg)O ₆ def.	400 w	404
	432 s	
	449 w	
	493 w	
	544 vw	
	562 w	
	644 w	
	668 s	
OH bending+Si-O-Mg bridging	681 vs	681
OH bending		884
OH bending		1036
	1140 w	
	1176 w	

Notes: Abbreviations: rot. = rotation; tr. = translation; def. = deformation; sym. = symmetric; w = weak; vw = very weak; s = strong; vs = very strong.

a From Borodina et al. (2020).

At the high-energy region 2850–3600 cm⁻¹, i.e., corresponding to the hydroxyl stretching region, we observe six distinct modes at ambient conditions. These six modes are located at 3461 cm⁻¹ (v_2^{OH}), 3402 cm⁻¹ (v_1^{OH}), 3289 cm⁻¹ (v_5^{OH}), 3225 cm⁻¹ (v_6^{OH}) , 3204 cm⁻¹ (v_4^{OH}) , and 3145 cm⁻¹ (v_3^{OH}) (Online Materials) Fig. OM4). Based on the first-principles simulation, 12 O-H stretching modes are predicted for the six distinct protons. This has also been reported in an earlier study (Wunder et al. 2012) (Fig. 3; Table 1). Infrared (IR) spectroscopic studies have revealed the presence of six O-H stretching modes at room temperature. It is likely that at high temperatures, owing to the disorder in proton motions or coupled OH motions, the vibrational modes are broadened and overlap such that instead of the 12 predicted modes, vibrational spectra show only six. However, upon cooling to -190 °C, at least eight hydroxyl modes were observed (Wunder et al. 2011, 2012). In our ambient spectra, the hydroxyl modes at the highest energies i.e., at 3461 cm⁻¹ (v_2^{OH}) and 3402 cm^{-1} (v_1^{OH}) are likely to be related to the shorter hydroxyl $(d_{\text{O-H}})$ bond lengths and longer hydrogen $(d_{\text{O-H-O}})$ bond distances that correlates with relatively weaker hydrogen bonds. The pair of hydroxyl and hydrogen bond lengths are similar for the H1 and H2 protons i.e., $d_{O1-H1} \sim 1.024$ Å and $d_{O1-H1} \sim 1.937$ Å; and d_{O2-H2} ~ 0.928 Å and $d_{O2\cdots H2} \sim 2.045$ Å and hence we assign v_1^{OH} and v₂^{OH} modes to O1-H1 and O2-H2 stretching vibrational modes, respectively (Online Materials¹ Table OM2). At relatively lower energy region, four additional modes are observed at 3289 cm⁻¹ (v_5^{OH}) , 3225 cm⁻¹ (v_6^{OH}) , 3204 cm⁻¹ (v_4^{OH}) , and 3145 cm⁻¹ (v_3^{OH}) . Owing to lower energy, these modes are likely related to shorter $d_{\text{O-H}}$ bond lengths and longer $d_{\text{H-O}}$ hydrogen bond lengths. The lowest energy mode 3145 cm⁻¹ (v_3^{OH}) is likely related to stronger hydrogen bonding and is assigned to the $d_{\text{O3}\text{--H4}} \sim 1.059 \text{ Å}$ and shorter $d_{\text{O4} \cdot \text{H6}} \sim 1.698 \text{ Å}$. The bond distances and the assignment of hydroxyl stretching modes are consistent with prior studies

(Wunder et al. 2011, 2012; Mookherjee et al. 2015).

The pressure dependence of the vibrational modes is adequately described by a second-order polynomial:

$$v_{i} = v_{i_0} + b_{i}P + c_{i}P^2$$

where, v_{i_0} is the mode frequency at ambient pressures, i.e., 0.1 MPa (10^{-4} GPa), b_i and C_i refers to dv_i/dP and d^2v_i/dP^2 , respectively (Table 2). The 3.65 Å phase becomes thermodynamically stable around ~9 GPa (Pawley et al. 2011) and the high-pressure stability limit of the 3.65 Å phase in a realistic mantle is dictated by the intersection of the subduction geotherms with the thermal stability of 3.65 Å phase, which is pressure insensitive (Pawley et al. 2011). This limits the maximum pressure stability at equilibrium to ~20 GPa (Online Materials¹ Fig. OM5). Thus, we conducted five distinct compressions: in two static compressions, we used alcohol mixtures as PTM and compressed up to ~20 GPa. In two additional static compressions, we used neon as PTM and compressed up to ~20 GPa. In an additional static compression with neon as PTM, we have explored pressures up to 60 GPa. Although we have explored high-pressure behavior up to ~60 GPa, we have analyzed the pressure dependence of all the modes to 20 GPa, the maximum pressure stability limit at equilibrium for 3.65 Å phase at the realistic mantle temperature (Table 2). Pressure dependence of modes up to the maximum pressure of 60 GPa, i.e., beyond the maximum pressure stability of 3.65 Å phase is presented in Online Materials¹ Table OM2. We note that even though the 3.65 Å phase in a realistic mantle will not be thermodynamically stable beyond 20 GPa. In our roomtemperature static compression measurements up to ~60 GPa, the 3.65 Å phase is likely to be in a metastable state.

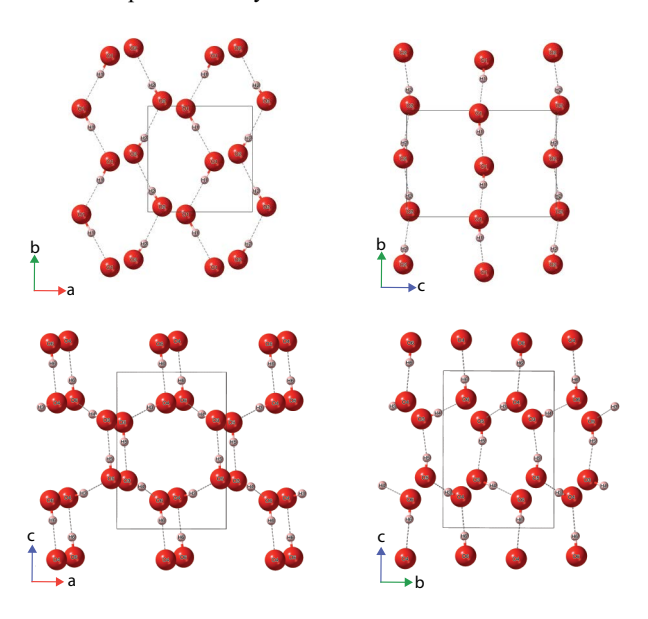


FIGURE 3. Hydrogen bond configurations: O1-H1···O1 is seen in the a-b plane i.e., projection down the c-axis; O2-H2···O2 is seen in the b-c plane, i.e., projection down the a-axis; O4-H3···O5, O3-H4···O6, O5-H5···O3, and O6-H6···O4 form a crank-shaft arrangement that is seen in the a-c plane, i.e., projection down the b-axis; similarly, the crank-shaft arrangement is also seen in the b-c plane, i.e., projection down the a-axis. (Color online.)

TABLE 2. Pressure-dependence of the Raman modes of the 3.65 Å phase and expansion coefficients

	This study						Borodina et al. (2020)			
Modes	ν _{i0} (cm ⁻¹)	σv_{i_0}	$b_{\scriptscriptstyle \mathrm{i}}$	$\sigma b_{\rm i}$	C _i	σς	V _{i0}	b_{i}	$\sigma b_{\scriptscriptstyle i}$	
1	198.4	1.0	3.80	0.22	-0.10	0.01	197	5.9	0.6	
2	203.9	0.5	5.48	0.15	-0.06	0.01				
3	226.0	1.1	3.89	0.33	-0.05	0.02				
4	238.5	0.6	4.68	0.28	-0.20	0.03				
5	245.8	0.3	4.11	0.20	-0.07	0.03				
5	264.8	1.1	1.98	0.32	-0.02	0.02	265	2.2	0.2	
7	269.8	17.5	0.80	2.55	0.12	0.09				Appears at 9.5 GPa
3	270.3	1.1	5.53	0.28	-0.06	0.01	271	5.2	0.5	• •
9	288.2	1.0	4.49	0.27	-0.02	0.01	290	4.3	0.4	
10	298.9	1.4	5.60	0.34	-0.09	0.02	300	5	0.5	
11	326.0	0.3	4.52	0.10	-0.06	0.01				
12	340.8	0.5	4.75	0.15	-0.08	0.01				
13	402.3	0.4	2.09	0.10	-0.01	0.01	404	1.9	0.2	
14	432.0	1.2	2.14	0.33	0.02	0.02				
15	446.2	3.3	1.93	0.90	0.09	0.05				
16	470.8	1.1	6.99	0.28	-0.09	0.02				
17	494.3	1.2	6.60	0.41	-0.07	0.02				
18	567.7	2.0	6.88	0.51	-0.06	0.03				
19	664.2	2.8	4.07	0.83	-0.06	0.04				
20	681.4	0.8	5.09	0.21	-0.04	0.01	681	5	0.5	
21	647.5	14.6	7.10	1.35	-0.08	0.03				Appears at 12 GPa
							884	4.1	0.4	
							1036	3.5	0.3	
22	1140.3	3.1	5.08	0.84	-0.06	0.04				
23	1182.7	2.6	6.58	0.76	-0.04	0.04				
24-OH-3	3144.4	3.0	-36.64	0.01	0.76	0.06	3147	-31.9	5.4	
								-8.6	5.8	4.7-6.5 GPa ^a
25-OH-4	3212.0	3.2	-26.00	0.01	0.52	0.15				
26-OH-6	3230.3	0.2	-9.51	0.10	-0.12	0.01				
27-OH-5	3287.5	2.4	-19.78	0.01	1.68	0.13	3291	-22.5	3.8	
								-2.2	6	5.6-6.5 GPa ^b
28-OH-1	3403.2	0.0	-9.37	0.01	0.06	0.00	3404	-9.3	0.9	
29-OH-2	3458.8	2.0	-4.97	0.50	-0.01	0.00	3463	-5.7	0.6	

Notes: Subscript "i" refers to the vibrational modes. The pressure dependence of the modes is described by an expansion of the form $v_i = v_{i_0} + b_i P + c_i P^2$ where b_i refers to the first derivative dv_i/dP and c_i refers to the second derivative d^2v_i/dP^2 . The v_{i_0} is the mode frequency at P_0 of 1×10^{-4} GPa. Errors represent 1σ uncertainties. The polynomial fit of the pressure dependence of the modes is carried out up to 20 GPa, i.e., within the stability field of 3.65 Å phase. The polynomial fit up to ~60 GPa is provided in the supporting information. Borodina et al. (2020) observed a slope change for $v_3^{\rm PH}$ mode 3147 cm⁻¹ at *4.7 GPa and $v_5^{\rm PH}$ mode 3291 cm⁻¹ at *5.6 GPa.

We observe that in the lattice energy region (180–1200 cm⁻¹), vibrational modes persist up to pressures ~60 GPa, with most of the modes exhibiting $b_i^{\text{lattice}} > 0$ and $c_i^{\text{lattice}} > 0$ (Figs. 4 and 5; Table 2). We do not find any indication of phase transition up to ~60 GPa from the pressure evolution of the deconvoluted modes. In the hydroxyl stretching region the O-H modes also exhibit pressure-induced changes including significant broadening and red-shift of all the modes, i.e., $b_i^{OH} < 0$ (Fig. 6; Table 2). We find the ν_3^{OH} and ν_4^{OH} modes exhibit the most pressure-induced red-shift with $b_3^{OH} = -36.64 \pm 0.01$ cm⁻¹/GPa and $b_4^{OH} = -26.00$ \pm 0.01 cm⁻¹/GPa. At ambient conditions, the v_3^{OH} and v_4^{OH} modes are related to the shortest $d_{\text{H---O}}$ distance, and upon compression, the hydrogen bonding is strengthened, which leads to further shortening of the $d_{\text{H-O}}$ distance. In contrast to the v_3^{OH} and v_4^{OH} modes, the v_2^{OH} mode is associated with the longest d_{H-O} distance, $d_{\text{H2} \cdot \cdot \cdot \text{O2}} \sim 2.045 \text{ Å}$, i.e., the weakest hydrogen bonding. As a result, it softens the least with $b_2^{OH} = -4.97 \pm 0.5$ cm⁻¹/GPa (Table 2). Compression beyond 5 GPa results in a drastic reduction of all the mode intensities. We find that at pressures >5.9 GPa, we are unable to detect the v_4^{OH} mode. This is followed by the disappearance of the v_5^{OH} and v_6^{OH} modes and at pressures >9.3 GPa we are unable to detect the v_3^{OH} mode. We note that only the v_1^{OH} and v_2^{OH} modes persist beyond 20 GPa and up to the pressure of ~60 GPa. Since we explored pressures beyond the hydrostatic limit of methanol:ethanol mixture, we repeated our study with neon as a PTM. To assess the effects of non-hydrostaticity we have used the full width at half-maxima (FWHM) of the v_1^{OH}

and v_2^{OH} modes (Online Materials¹ Fig. OM6). We find good agreement between the distinct experimental runs where samples were loaded with the different PTM. An increase in the stressed-induced width broadening is expected with the methanol:ethanol mixture beyond its hydrostatic limit i.e., ~10 GPa (Angel et al. 2007). In our study, we note mode broadening of $\Gamma_{v_l}^{OH}$ and $\Gamma_{v_l}^{OH}$ at pressures >5 GPa and this is likely due to enhanced proton

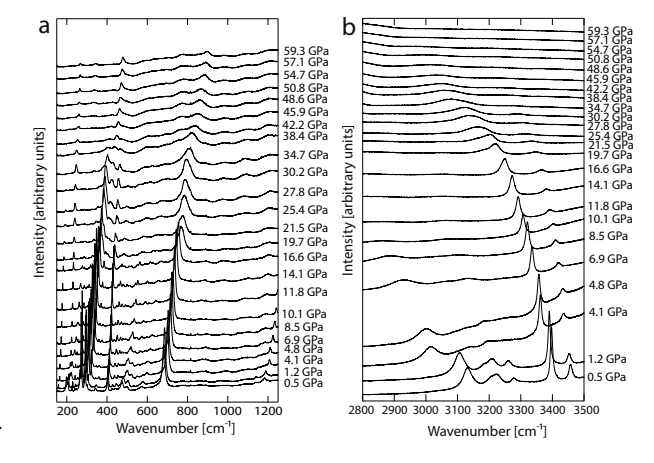


FIGURE 4. (a) Pressure-dependent Raman spectra of the low-wavenumber region ~150–1250 cm⁻¹ of the 3.65 Å phase. (b) Pressure-dependent Raman spectra of the hydroxyl stretching region ~2850–3550 cm⁻¹ of the 3.65 Å phase.

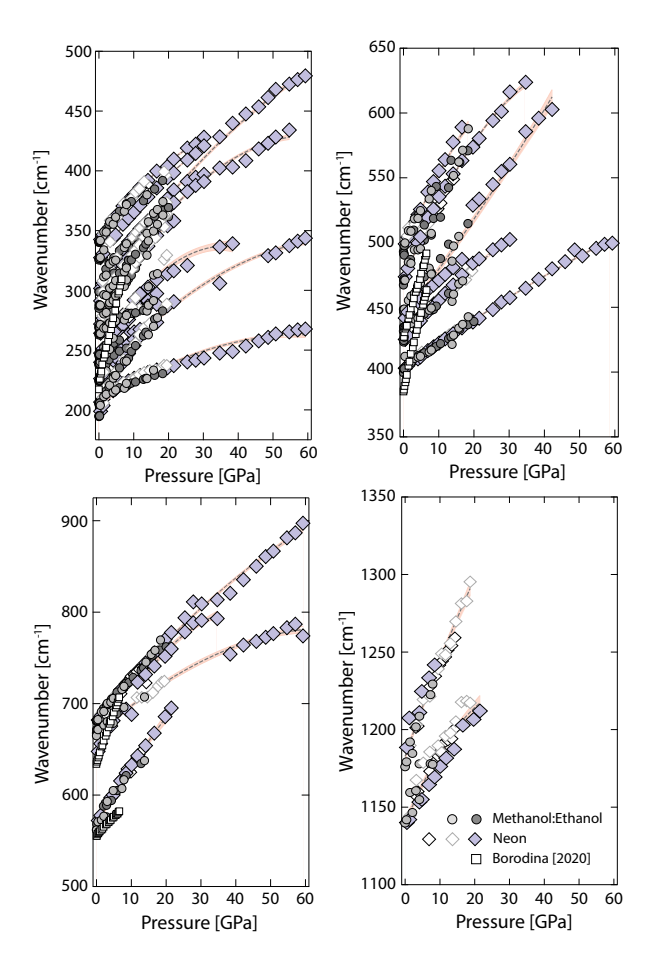


FIGURE 5. Pressure dependence of the vibrational mode frequencies of the 3.65 Å phase in the low-energy region. Deconvoluted mode frequencies from five compressional runs using two different pressure media are overlain. The pressure dependence of the modes is adequately described by a polynomial expression shown as a dashed line. The fit parameters v_{i0} , b_{i} , and c_{i} , within the high-pressure stability limit (Online Materials1 Fig. OM5) i.e., for pressure dependence up to 20 GPa is reported in Table 2. The fit parameters v_{i0} , b_{i} , and c_{i} , beyond the high-pressure stability limit (Online Materials¹ Fig. OM5) i.e., for pressure dependence up to 60 GPa is reported in Online Materials¹ Table OM3. (Color online.)

disorder often observed in hydrous minerals at high pressures (Tsuchiya et al. 2005). Upon compression beyond 30 GPa, we observe a significant increase in the full width of half maxima of the modes. The pressure-induced broadening is accompanied by a decrease in the mode intensity. The v_1^{OH} and v_2^{OH} modes were indistinguishable from the baseline at the highest pressures explored i.e., 55–60 GPa and deconvolution results in significant errors in both energy of the modes and the full width of half maxima.

To better understand the relation between the hydroxyl stretching modes, v_i^{OH} of the 3.65 Å and its pressure derivatives, b_i^{OH} , we compare results from our study with that of other relevant hydrous phases (Fig. 7). We note that the pressure derivatives, b_i^{OH} of the hydroxyl modes increase linearly with the mode frequency v_i^{OH} for most of the hydrous phases including the 3.65 Å phase. For compressible layered hydrous silicate minerals such as serpentine polymorphs, lizardite, antigorite, chrysotile, talc,

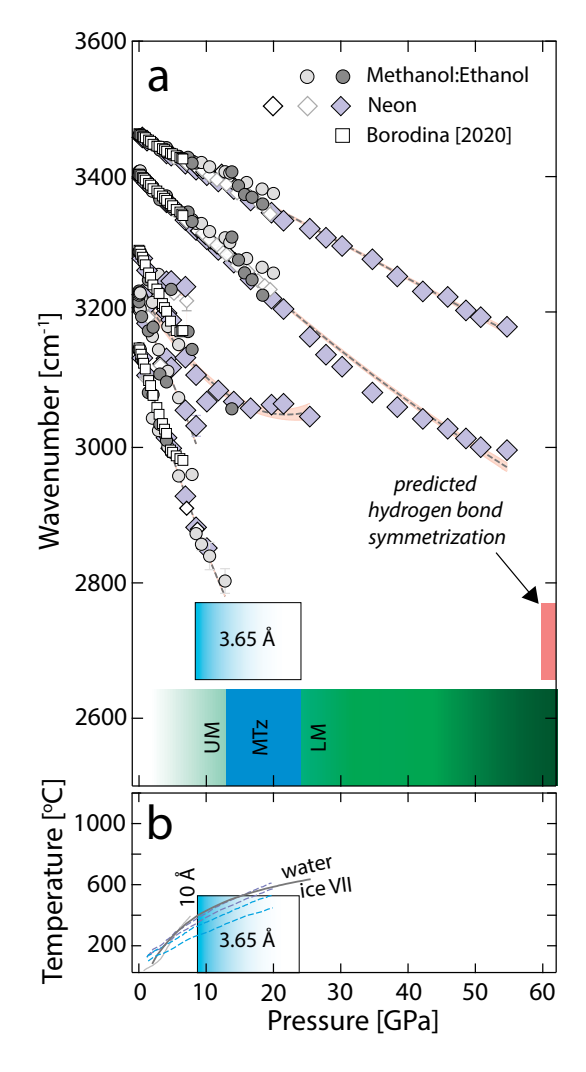


FIGURE 6. (a) Plot of the pressure dependence of the vibrational mode frequencies of the 3.65 Å phase in the hydroxyl stretching region. Deconvoluted mode frequencies from five compressional runs using two different PTM. The pressure dependence of the modes is adequately described by a polynomial expression shown as a dashed line. The fit parameters v_{i0} , b_i , and c_i , within the high-pressure stability limit (Online Materials1 Fig. OM5) i.e., for pressure dependence up to 20 GPa is reported in Table 2. The fit parameters v_{i_0} , b_i , and c_i , beyond the high-pressure stability limit (Online Materials1 Fig. OM5) i.e., for pressure dependence up to 60 GPa is reported in Online Materials¹ Table OM3. The shaded regions indicate the stability of the 3.65 Å phase (blue gradient), the predicted hydrogen bond symmetrization (pink), upper mantle (UM: light green gradient), mantle transition zone (MTZ: blue), and lower mantle (LM: dark green gradient). (b) The 3.65 Å phase forms at around ~9 GPa (Pawley et al. 2011). The 3.65 Å phase is not thermodynamically stable below 9 GPa (Pawley et al. 2011). The high-pressure stability limit of 3.65 Å phase in a realistic mantle is dictated by the intersection of the subduction geotherms with the thermal stability of 3.65 Å phase, which is pressure insensitive (Pawley et al. 2011). The thermodynamic stability region of the 3.65 Å phase is indicated by a shaded region (blue gradient). The solid dark gray line indicates the water-ice VII phase boundary. The solid light gray line indicates Tonga slab geotherm (Syracuse et al. 2010). The dashed lines indicate the lowest temperature predicted in the Tonga slab (Bina and Navrotsky 2000). (Color online.)

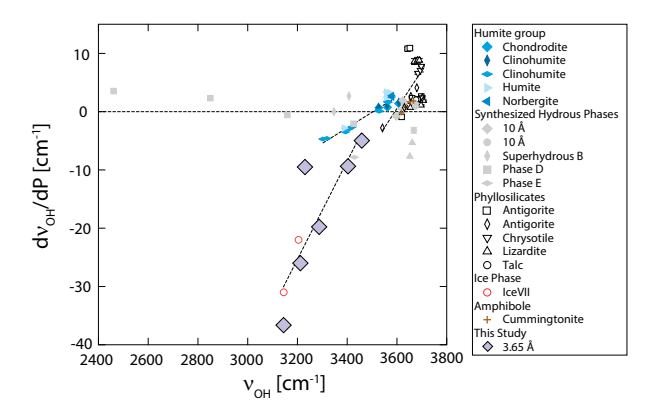


FIGURE 7. The pressure dependence of hydroxyl stretching mode frequency, b_i^{OH} with OH-stretching mode frequency, v_i^{OH} at ambient condition, i.e., 1 bar, for different hydrous mineral phases in the MSH ternary system. Reference for mineral phases: Chondrodite (Liu et al. 2003); Clinohumite (Liu et al. 2003, 2021); Humite (Liu et al. 2021); Norbergite (Liu et al. 2021); 10 Å (Comodi et al. 2007; Parry et al. 2007); Superhydrous B (Koch-Müller et al. 2005); Phase D (Shieh et al. 2009); Phase E (Kleppe et al. 2001); Serpentine: Antigorite (Auzende et al. 2004; Noguchi et al. 2012); Serpentine: Chrysotile (Auzende et al. 2004); Serpentine: Lizardite (Auzende et al. 2004); Talc (Scott et al. 2007); Ice VII (Hsieh and Chien 2015); Cummingtonite (Yang et al. 1998). (Color online.)

and 10 Å phase that has softer bulk moduli, exhibit the steepest trends in the $b_i^{\rm OH}$ vs. $v_i^{\rm OH}$. Hydrous phases such as the 3.65 Å phase exhibit an intermediate trend in $b_i^{\rm OH}$ vs. $v_i^{\rm OH}$. Hydrous phases such as superhydrous phase B, humite group, chondrodite, and norbergite have relatively stiffer bulk moduli and thus exhibit a flatter trend in $b_i^{\rm OH}$ vs. $v_i^{\rm OH}$. The dense hydrous phase D shows a slight negative trend in $b_i^{\rm OH}$ vs. $v_i^{\rm OH}$ with $b_i^{\rm OH}$ remaining mostly insensitive to $v_i^{\rm OH}$. The overall correlation of compressibility with $b_i^{\rm OH}$ trend is consistent with the dependency of $v_i^{\rm OH}$ on $d_{\rm O-H-O}$ distances which change more rapidly with pressure in compressible solids such as micas and hydroxides.

The OH-stretching frequency of the hydrous minerals is sensitive to the interaction of the proton with its environment to second-, third- and even fourth-nearest-neighbors. The v_i^{OH} is often strongly correlated with hydrogen bond $d_{\text{O-H-O}}$ distances (Libowitzky 1999; Goryainov 2012) (Online Materials¹ Fig. OM7). Longer hydrogen bond distances $d_{\text{O-H-O}}$ are often related to stronger and shorter OH bonds with v_i^{OH} shifted to higher energies. However, upon compression, these longer hydrogen bond distances often undergo shortening, which results in enhanced hydrogen bonds and weakening of OH bond, and significant red shift of the v_i^{OH} with b_i^{OH} <0. In 3.65 Å phase, we note that the magnitude of b_i^{OH} <0 increases with decreasing v_i^{OH} . This likely indicates that the hydrogen bond lengths are shorter at higher pressures (Fig. 7; Table 2).

DISCUSSION

It is well known that hydrous mineral phases play a vital role in transporting water into the deep Earth. To provide a better geophysical constraint on the degree of mantle hydration, it is thus crucial to have better constraints on the elastic properties of such hydrous phases. The parameters that influence bulk seismic velocities of mineral aggregates are the modal abundance of the individual mineral phases, the elasticity of individual mineral phases, and the lattice preferred orientation. Thus, detecting the degree of mantle hydration is dependent on the modal abundance, elasticity, and the lattice preferred orientation of the hydrous phase under extreme conditions. While it could be argued that water in the deep mantle is mostly sequestered in nominally anhydrous minerals and thus the modal abundance of the hydrous phase is likely to be relatively low. Evidence of hydrous phase inclusions within diamonds (Wirth et al. 2007; Keppler 2014; Lovett 2014; Pearson et al. 2014) and ice-VII phase indicating potential supercritical aqueous fluid inclusion within diamonds (Tschauner et al. 2018) from subduction zone settings indicate that hydrous phases are indeed present in the deeply subducted slabs and help in transporting water into the deep Earth. Clearly, constraints on all these parameters are poor for many of the hydrous phases that are experimentally found to be stable at high pressures and temperatures relevant to subduction zone conditions. In addition to all these parameters, there is an additional parameter that could further complicate the detection of the degree of mantle hydration and this is related to the fact that most hydrous phases often undergo pressure-induced strengthening of hydrogen bonds and eventually hydrogen-bond symmetrization. Such hydrogen bond symmetrizations have been reported in dense hydrous phases including phase D (Tsuchiya et al. 2002), phase-H (Tsuchiya and Mookherjee 2015), phase-Egg (Mookherjee et al. 2019), and δ-AlOOH (Panero and Stixrude 2004; Tsuchiya et al. 2005; Sano-Furukawa et al. 2008). Hydrogen bond symmetrization is known to have a significant effect on the elastic moduli of the hydrous phases. Often such pressure-induced hydrogen-bond symmetrization leads to stiffening of bulk and shear moduli such that the hydrous phase becomes indistinguishable from volumetrically abundant nominally anhydrous mantle minerals. Thus pressure-induced hydrogen-bond symmetrization often makes it difficult to detect mantle hydration via bulk seismological observations.

First-principles simulations based on density functional theory have predicted symmetrization of hydrogen bond and thus likely stiffening of elasticity for 3.65 Å phase at ~60 GPa (Mookherjee et al. 2015). Although the 3.65 Å phase becomes stable at 9.0 GPa, its high-pressure stability limit is poorly constrained (Wunder et al. 2011). It has very limited temperature stability of ~500 °C, that is insensitive to pressure (Wunder et al. 2011). At pressures corresponding to predicted symmetrization, i.e., 60 GPa, even the coldest geotherm is likely to exceed ~500 °C. Thus, the predicted symmetrization of the hydrogen bond for the 3.65 Å phase is likely to exceed its thermodynamic stability. However, DFT-based simulations often fail to adequately address light elements such as hydrogen, as recently documented by considering thermal and nuclear quantum effects (Bronstein et al. 2017). Hence, we explored the high-pressure behavior of the OH region using Raman spectroscopy to assess pressure-induced changes in the hydrogen bonds. Ice phases are known to undergo hydrogen-bond symmetrization at high pressures, and previous studies on protonated and deuterated ices have revealed a phase transition at 60 GPa identified from a soft-mode-like behavior of the OH- or OD-stretching mode

Mineral/phase	Formula	ρ₀ (g/cm³)	K_0 (GPa)	K' ₀	K_0/K_0' (GPa)	H₂O (wt%)	Reference
		Dense hydro	us magnesii	um silica	tes (DHMS)		
3.65 Å phase	MgSi(OH) ₆	2.636	84	4.9	17.1	35	Mookherjee et al. (2015)
Clinohumite	$Mg_9Si_4O_{16}(OH)_2$	3.187	119.4	4.8	24.9	2.9	Ross and Crichton (2001)
Chondrodrite	$Mg_5Si_2O_8(OH)_2$	3.057	115.7	4.9	23.6	5.3	Ross and Crichton (2001)
Phase A	Mg ₇ Si ₂ O ₈ (OH) ₆	2.976	106	5.8	18.3	11.84	Sanchez-Valle et al. (2008)
Phase B	$Mg_{12}Si_4O_{19}(OH)_2$	3.368	163	4.0	40.8	2.43	Finger et al. (1989); Kudoh et al. (1995)
Superhydrous phase B	$Mg_{10}Si_3O_{10}(OH)_4$	3.327	154	4.0	38.5	6.49	Gerald Pacalo and Weidner (1996)
Phase D	$MgSi_2H_2O_6$	3.459	166	4.1	40.5	18.49	Frost and Fei (1999)
Phase E	$Mg_{2,23}Si_{1,81}H_{2,8}O_6$	2.92	93	5.0	18.6	13.6	Shieh et al. (2000)
		Layered hydro	ous magnes	ium silio	ates (LHMS)		
Brucite	Mg(OH)₂	2.38	43.8	6.8	6.4	30.89	Jiang et al. (2006)
Serpentine	Mg₃Si₂O₅(OH)₄	2.62	61	6.7	9.1	13	Bezacier et al. (2013)
Talc	$Mg_3Si_4O_{10}(OH)_2$	2.75	41	6.0	6.8	4.75	Pawley et al. (2002)
10 Å phase	$Mg_3Si_4O_{10}(OH)_2\cdot H_2O$	2.676	39	12.5	3.1	9.5	Comodi et al. (2006)
		Mantle phases a	ind nominal	lly anhy	drous minerals		
Olivine	Mg₂SiO₄	3.218	125.5	4.0	31.4	0	Downs et al. (1996)
Clinoenstatite	MgSiO₃	3.301	155	5.5	28.2	0	Kung (2005)
Majorite	MgSiO₃	3.522	159.8	5.8	27.6	0	Gerald Pacalo and Weidner (1997)
Bridgmanite	MgSiO₃	4.098	256.7	4.1	62.6	0	Yagi et al. (1978); Tange et al. (2012)
Hydrous olivine	Mg₂SiO₄	3.18	125.4	4.5	27.9	0.9	(Mao et al. 2010)
Hydrous wadsleyite	β-Mg₂SiO₄	3.435	161.3	4.1	39.3	0.84	(Mao et al. 2008)
Hydrous ringwoodite	γ-Mg₂SiO₄	3.649	175.2	4.0	43.8	1.1	(Mao et al. 2012)

TABLE 3. Density, bulk modulus, and water content for various hydrous minerals and phases in the MSH ternary

 $(b_i^{OH} < 0)$ below the transition followed by a positive pressuredependence $(b_i^{OH} > 0)$ above the transition pressure (Goncharov et al. 1996). The shift in the pressure dependence of the stretching mode is generally interpreted as the transformation of the ice-VII phase to a crystal structure with symmetrized hydrogen bonds. In the present study, as predicted from simulations, the hydrogen bond strength enhances under compression up to ~60 GPa i.e., $b_i^{OH} < 0$, however, the pressure evolution of the OHstretching modes does not reveal any reversal in the pressure dependence. At the highest pressures explored, i.e., 55-60 GPa, the v_1^{OH} and v_2^{OH} modes were indistinguishable from the baseline and deconvolution of results in significant errors in both energies of the modes and the full width of half maxima. Therefore, till the highest pressures explored in this study, i.e., 60 GPa, which is significantly higher than the high-pressure stability of 3.65 Å phase (Online Materials¹ Fig. OM5; Fig. 6), we were unable to validate the predicted hydrogen-bond symmetrization.

High-pressure Raman measurements and the pressure dependence of the vibrational modes may provide a valuable constraint on the ratio of bulk moduli to its pressure derivative that might hint toward the behavior of the hydrous phase at greater depth. We have attempted such analysis for the 3.65 Å phase and compared our estimates based on Raman spectroscopy with that of the equation of state studies. The comparisons are in good agreement, thus validating the strength of such analysis based on Raman measurements (Table 3). The ratio of bulk modulus and its pressure derivative, K_0/K_0' can be expressed in terms of the vibrational modes at ambient conditions (v_{i_0}) , first derivative, $b_i = dv_i/dP$, and second derivative, $c_i = d^2v_i/dP^2$, of the pressure dependence of the vibrational modes as:

$$\frac{K_0}{K_0'} = \left(\frac{b_i}{v_{i_0}} - \frac{2c_i}{b_i}\right)^{-1}$$

where bulk modulus (K_0) is related to v_{i_0} and b_i via the formalism $K_0 = \gamma_i (v_{i_0}/b_i)$, where γ_i is the Grüneisen parameter (Chopelas 1990; Hofmeister 1991; Liu 2002), and the pressure derivative of the bulk modulus (K'_0) is related to v_{i_0} , b_i , c_i , and γ_i via the formalism

$$K_0' = \gamma_i \left(1 - \frac{2v_{i_0}c_i}{b_i^2} \right).$$

For the 3.65 Å phase, we find $K_0/K_0'\sim 14.3\pm 5.5$ GPa (Online Materials¹ Table OM4) in agreement with the recent study (Mookherjee et al. 2015) (Fig. 8; Table 3). It is to be noted that determining K'_0 accurately from the equation of state studies is often challenging because it tends to exhibit a strong negative correlation with the bulk modulus (K_0) in the equation of state. Thus, the above-mentioned approach provides alternate constraints on K_0/K'_0 using the pressure dependence of vibrational modes (Table 3). We note that K_0/K_0' for the normal mantle phases and nominally anhydrous minerals in the simplified MgO-SiO₂-H₂O (MSH) ternary system are overall greater than the layered hydrous magnesium silicates (LHMS) and dense hydrous magnesium silicates (DHMS) (Table 3). Prior studies on other hydrous phases indicate overall trends that they are more compressible, which is likely to make their detection challenging at greater depths. Further studies on shear elastic moduli and elastic anisotropy are warranted for determining the degree of deep mantle hydration.

IMPLICATIONS

To provide better geophysical limits on the degree of mantle hydration, it is important to have good constraints on the elasticity of hydrous mineral phases. Most equation of state studies indicates that hydrous phases that are stable at relatively shallower depths, i.e., layered hydrous phases and hydroxides, often have lower bulk moduli (K_0) compared to that of the major mantle mineral phases. Based on our high-pressure Raman study on 3.65 Å phase, we do not observe any evidence for structural changes associated with the MgO6 and SiO6 octahedral framework, we do observe the strengthening of hydrogen bonds, but we were unable to validate the symmetrization of hydrogen bonding up to pressures of 60 GPa. This is beyond the maximum pressure stability of 3.65 Å phase, considering equilibrium thermodynamics. It is well known that symmetrization of hydrogen bonding is often associated with further stiffening of elastic parameters. Thus based on our study, we do not anticipate such stiffening

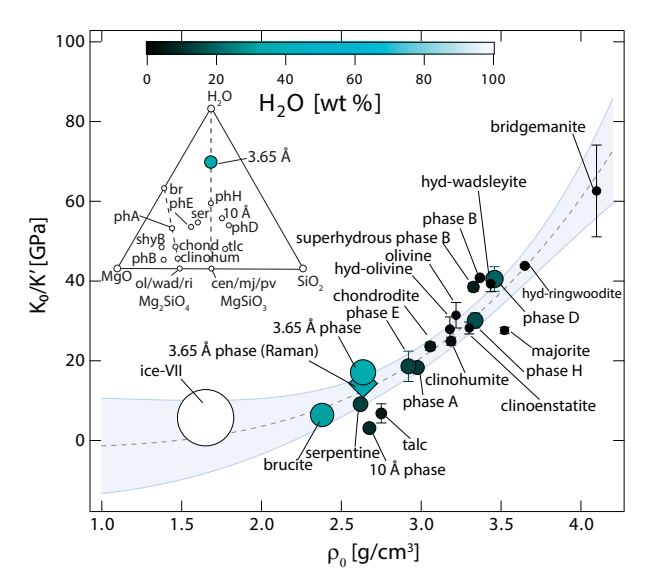


FIGURE 8. The plot shows a systematic relation between the ratio of bulk moduli, K_0 to its pressure derivative, K'_0 i.e., K_0/K'_0 and density (ρ) systematics for various hydrous mineral phases in MSH ternary system. The K_0/K_0' and density data (ρ) for the mineral phases are colored based on their water content. The systematic relation is best described by a power function shown in by gray dashed line $(K_0/K_0') = (K_0/K_0')_0 + A\rho''$, where, K_0/K_0' $\sim -1.8114 \pm 13.0$, $A \sim 0.45716 \pm 1.08$, and $n \sim 3.5491 \pm 1.62$. The confidence band is shown in light blue shading. The filled sphere represents data from X-ray diffraction (Table 3). The filled rhomb represents K_0/K'_0 for 3.65 Å phase deduced from pressure dependence of Raman data (this study; Online Materials¹ Table OM4). The darker symbols represent lower or no water content, whereas lighter symbols represent mineral phases that are richer in H₂O wt%. The horizontal color scale shows the H₂O wt%. The color scale helps to distinguish the dry, nominally anhydrous, and hydrous phases. The symbol sizes are also proportional to water content i.e., the darker symbols are smaller in size, and lighter symbols are larger in size. The ternary diagram (in mol%) modified from (Wunder et al. 2012; Mookherjee et al. 2015) is also shown with various hydrous phases in the MgO-SiO₂-H₂O (MSH) system, including 3.65 Å phase. Mineral abbreviations and stoichiometry: br = brucite $[Mg(OH)_2]$, tlc = talc $[Mg_3Si_4O_{10}(OH)_2]$; 10 Å = 10 Å phase $[Mg_3Si_4O_{10}(OH)_2 \cdot H_2O]$, 3.65 Å = 3.65 Å phase $[MgSi(OH)_6]$, clinohum clinohumite $[Mg_9Si_4O_{16}(OH)_2]$, chond = chondrodite $[Mg_5Si_2O_8(OH)_2]$, $phA = phase A [Mg_7Si_2O_8(OH)_6], phB = phase B [Mg_{12}Si_4O_{19}(OH)_2], phH$ = phase H [MgSiO₄H₂], phD = phase D [MgSi₂H₂O₆], phE = phase E $[Mg_{2}, Si_{1}, Si_{1}, H_{2}, O_{6}]$, cen = clinoenstatite $[MgSiO_{3}]$, mj = majorite $[MgSiO_{3}]$, pv = bridgmanite/perovskite [MgSiO₃], ol = olivine [Mg₂SiO₄], wad = wadsleyite [β -Mg₂SiO₄], ri = ringwoodite [γ -Mg₂SiO₄], ser = serpentine $[Mg_3Si_2O_5(OH)_4]$, and $ShyB = superhydrous phase B <math>[Mg_{10}Si_3O_{10}(OH)_4]$. (Color online.)

of at least up to 60 GPa. Another key parameter is the pressure derivative of the bulk moduli (K_0) that dictates compressibility at greater depths. Although relatively more compressible at lower pressures, hydrous phases and nominally anhydrous phases have greater compressibility than that of anhydrous or dry mantle phases (Jacobsen 2006). Thus, at conditions relevant to the mantle, the bulk moduli of dry mantle phases and hydrous phases may become indistinguishable. In contrast to the layered hydrous phases, the dense hydrous magnesium silicates and similarly structured mineral phases often have stiffer bulk moduli. Although to fully evaluate the degree of mantle hydra-

tion, better constraints on both bulk and shear moduli are needed, often the first step is to constrain the fundamental elastic moduli using the equation of state studies. For hydrous phases that are synthesized using high-pressure experiments, such data may or may not be available.

ACKNOWLEDGMENTS AND FUNDING

The authors thank an anonymous reviewer, Mark Welch, and the associate editor Susannah Dorfman for their constructive criticism, which was extremely helpful in adding clarity. This work is funded by the National Science Foundation (NSF) (EAR 1753125 and 1638752). A.B. acknowledges the Dean's Postdoctoral Scholar Fellowship from the College of Arts and Sciences, Florida State University. M.M. and A.B. acknowledge computing resources from XSEDE/ACCESS facilities (GEO170003) and the High-Performance Computing, Research Computing Center, Florida State University. Use of the COMPRES-GSECARS gas loading system was supported by COMPRES under NSF Cooperative Agreement EAR -1606856 and by GSECARS through NSF grant EAR-1634415 and DOE grant DE-FG02-94ER14466. This research used resources of the Advanced Photon Source, a U.S. Department of Energy (DOE) Office of Science User Facility operated for the DOE Office of Science by Argonne National Laboratory under Contract No. DE-AC02-06CH11357.

REFERENCES CITED

Angel, R.J., Bujak, M., Zhao, J., Gatta, G.D., and Jacobsen, S.D. (2007) Effective hydrostatic limits of pressure media for high-pressure crystallographic studies. Journal of Applied Crystallography, 40, 26–32, https://doi.org/10.1107/S0021889806045523.

Auzende, A.-L., Daniel, I., Reynard, B., Lemaire, C., and Guyot, F. (2004) High-pressure behaviour of serpentine minerals: A Raman spectroscopic study. Physics and Chemistry of Minerals, 31, 269–277, https://doi.org/10.1007/s00269-004-0384-0.

Basu, A. and Mookherjee, M. (2021) Intercalation of water in kaolinite (Al₂Si₂O₅(OH)₄) at subduction zone conditions: Insights from Raman spectroscopy. ACS Earth & Space Chemistry, 5, 834–848, https://doi.org/10.1021/acsearthspacechem.0c00349.

Bezacier, L., Reynard, B., Cardon, H., Montagnac, G., and Bass, J.D. (2013) High-pressure elasticity of serpentine and seismic properties of the hydrated mantle wedge. Journal of Geophysical Research. Solid Earth, 118, 527–535, https://doi.org/10.1002/jgrb.50076.

Bina, C.R. and Navrotsky, A. (2000) Possible presence of high-pressure ice in cold subducting slabs. Nature, 408, 844–847, https://doi.org/10.1038/35048555.

Borodina, U., Goryainov, S., Oreshonkov, A., Shatskiy, A., and Rashchenko, S. (2020) Raman study of 3.65 Å-phase MgSi(OH)₆ under high pressure and the bands assignment. High Pressure Research, 40, 495–510, https://doi.org/10.1080/08957959.2020.1830078.

Bronstein, Y., Depondt, P., and Finocchi, F. (2017) Thermal and nuclear quantum effects in the hydrogen bond dynamical symmetrization phase transition of δ-AIOOH. European Journal of Mineralogy, 29, 385–395, https://doi.org/10.1127/ eim/2017/0029-2628.

Chopelas, A. (1990) Thermal properties of forsterite at mantle pressures derived from vibrational spectroscopy. Physics and Chemistry of Minerals, 17, 149–156, https:// doi.org/10.1007/BF00199666.

Comodi, P., Cera, F., Dubrovinsky, L., and Nazzareni, S. (2006) The high-pressure behaviour of the 10 Å phase: A spectroscopic and diffractometric study up to 42 GPa. Earth and Planetary Science Letters, 246, 444–457, https://doi.org/10.1016/j. epsl.2006.03.046.

Comodi, P., Cera, F., Nazzareni, S., and Dubrovinsky, L. (2007) Raman spectroscopy of the 10 Å phase at simultaneously HP-HT. European Journal of Mineralogy, 19, 623–629, https://doi.org/10.1127/0935-1221/2007/0019-1753.

Downs, R.T., Zha, C.S., Duffy, T.S., and Finger, L.W. (1996) The equation of state of forsterite to 17.2 GPa and effects of pressure media. American Mineralogist, 81, 51–55, https://doi.org/10.2138/am-1996-1-207.

Fei, Y., Ricolleau, A., Frank, M., Mibe, K., Shen, G., and Prakapenka, V. (2007) Toward an internally consistent pressure scale. Proceedings of the National Academy of Sciences, 104, 9182–9186, https://doi.org/10.1073/pnas.0609013104.

Finger, L.W., Ko, J., Hazen, R.M., Gasparik, T., Hemley, R.J., Prewitt, C.T., and Weidner, D.J. (1989) Crystal chemistry of phase B and an anhydrous analogue: Implications for water storage in the upper mantle. Nature, 341, 140–142, https:// doi.org/10.1038/341140a0.

Frost, D.J. and Fei, Y. (1999) Static compression of the hydrous magnesium silicate phase D to 30 GPa at room temperature. Physics and Chemistry of Minerals, 26, 415–418, https://doi.org/10.1007/s002690050202.

Gerald Pacalo, R.E. and Weidner, D.J. (1996) Elasticity of superhydrous B. Physics and Chemistry of Minerals, 23, 520–525.

———(1997) Elasticity of majorite, MgSiO₃ tetragonal garnet. Physics of the Earth and Planetary Interiors, 99, 145–154, https://doi.org/10.1016/S0031-9201(96)03158-5. Goncharov, A.F., Struzhkin, V.V., Somayazulu, M.S., Hemley, R.J., and Mao, H.K. (1996) Compression of ice to 210 gigapascals: Infrared evidence for a sym-

metric hydrogen-bonded phase. Science, 273, 218-220, https://doi.org/10.1126/

- science.273.5272.218.
- Goryainov, S.V. (2012) A model of phase transitions in double-well Morse potential: Application to hydrogen bond. Physica B, Condensed Matter, 407, 4233–4237, https://doi.org/10.1016/j.physb.2012.06.045.
- Hirschmann, M.M. (2006) Water, melting, and the deep Earth H₂O cycle. Annual Review of Earth and Planetary Sciences, 34, 629–653, https://doi.org/10.1146/ annurev.earth.34.031405.125211.
- Hofmeister, A.M. (1991) Calculation of bulk modulus and its pressure derivatives from vibrational frequencies and mode Grüneisen Parameters: Solids with cubic symmetry or one nearest-neighbor distance. Journal of Geophysical Research, 96 (B10), 16181, https://doi.org/10.1029/91JB01381.
- Hohenberg, P. and Kohn, W. (1964) Inhomogeneous electron gas. Physical Review, 136 (3B), B864–B871, https://doi.org/10.1103/PhysRev.136.B864.
- Hsieh, W.-P. and Chien, Y.-H. (2015) High pressure Raman spectroscopy of H₂O-CH₃OH mixtures. Scientific Reports, 5, 8532, https://doi.org/10.1038/srep08532.
- Iwamori, H. (1998) Transportation of H₂O and melting in subduction zones. Earth and Planetary Science Letters, 160, 65–80, https://doi.org/10.1016/S0012-821X(98)00080-6.
- ———(2004) Phase relations of peridotites under H₂O-saturated conditions and ability of subducting plates for transportation of H₂O. Earth and Planetary Science Letters, 227, 57–71, https://doi.org/10.1016/j.epsl.2004.08.013.
- ——— (2007) Transportation of H₂O beneath the Japan arcs and its implications for global water circulation. Chemical Geology, 239, 182–198, https://doi.org/10.1016/j. chemgeo.2006.08.011.
- Jacobsen, S.D. (2006) Effect of water on the equation of state of nominally anhydrous minerals. Reviews in Mineralogy and Geochemistry, 62, 321–342, https://doi.org/ 10.2138/rmg.2006.62.14.
- Jahn, S., Wunder, B., Koch-Müller, M., Tarrieu, L., Pöhle, M., Watenphul, A., and Taran, M.N. (2012) Pressure-induced hydrogen bond symmetrisation in guyanaite, β-CrOOH: Evidence from spectroscopy and ab initio simulations. European Journal of Mineralogy, 24, 839–850, https://doi.org/10.1127/0935-1221/2012/0024-2228.
- Jiang, F., Speziale, S., and Duffy, T.S. (2006) Single-crystal elasticity of brucite, Mg(OH)₂, to 15 GPa by Brillouin scattering. American Mineralogist, 91, 1893–1900, https://doi.org/10.2138/am.2006.2215.
- Karato, S. (2010) Rheology of the Earth's mantle: A historical review. Gondwana Research, 18, 17–45, https://doi.org/10.1016/j.gr.2010.03.004.
- Kawamoto, T. (2006) Hydrous phases and water transport in the subducting slab. Reviews in Mineralogy and Geochemistry, 62, 273–289, https://doi.org/10.2138/ rmg.2006.62.12.
- Keppler, H. (2014) Earth's deep water reservoir. Nature, 507, 174–175, https://doi.org/ 10.1038/507174a.
- Kleppe, A.K., Jephcoat, A.P., and Ross, N.L. (2001) Raman spectroscopic studies of phase E to 19 GPa. American Mineralogist, 86, 1275–1281, https://doi.org/10.2138/ am-2001-1015.
- Kleppe, A.K., Welch, M.D., Crichton, W.A., and Jephcoat, A.P. (2012) Phase transitions in hydroxide perovskites: A Raman spectroscopic study of stottite, FeGe(OH)₆, to 21 GPa. Mineralogical Magazine, 76, 949–962, https://doi.org/10.1180/ minmag.2012.076.4.11.
- Klotz, S., Chervin, J.-C., Munsch, P., and Le Marchand, G. (2009) Hydrostatic limits of 11 pressure transmitting media. Journal of Physics D, Applied Physics, 42, 075413, https://doi.org/10.1088/0022-3727/42/7/075413.
- Koch-Müller, M., Dera, P., Fei, Y., Hellwig, H., Liu, Z., Van Orman, J., and Wirth, R. (2005) Polymorphic phase transition in Superhydrous Phase B. Physics and Chemistry of Minerals, 32, 349–361, https://doi.org/10.1007/s00269-005-0007-4.
- Koch-Müller, M., Appelt, O., Wunder, B., and Wirth, R. (2021) New insights in the mechanisms of the reaction 3.65 Å phase = clinoenstatite + water down to nanoscales. European Journal of Mineralogy, 33, 675–686, https://doi.org/10.5194/ ejm-33-675-2021.
- Kohn, W. and Sham, L.J. (1965) Self-Consistent Equations Including Exchange and Correlation Effects. Physical Review, 140(4A), A1133–A1138, https://doi.org/10.1103/PhysRev.140.A1133.
- Kresse, G. and Furthmüller, J. (1996a) Efficiency of ab-initio total energy calculations for metals and semiconductors using a plane-wave basis set. Computational Materials Science, 6, 15–50, https://doi.org/10.1016/0927-0256(96)00008-0.
- ———(1996b) Efficient iterative schemes for ab initio total-energy calculations using a plane-wave basis set. Physical Review B: Condensed Matter, 54, 11169–11186, https://doi.org/10.1103/PhysRevB.54.11169.
- Kresse, G. and Hafner, J. (1993) Ab initio molecular dynamics for liquid metals. Physical Review B: Condensed Matter, 47, 558–561, https://doi.org/10.1103/ PhysRevB.47.558.
- Kresse, G. and Joubert, D. (1999) From ultrasoft pseudopotentials to the projector augmented-wave method. Physical Review B: Condensed Matter, 59, 1758–1775, https://doi.org/10.1103/PhysRevB.59.1758.
- Kudoh, Y., Nagase, T., Sasaki, S., Tanaka, M., and Kanzaki, M. (1995) Phase F, a new hydrous magnesium silicate synthesized at 1000 °C and 17 GPa: Crystal structure and estimated bulk modulus. Physics and Chemistry of Minerals, 22, 295–299, https://doi.org/10.1007/BF00202769.
- Kung, J. (2005) In-situ elasticity measurement for the unquenchable high-pressure clinopyroxene phase: Implication for the upper mantle. Geophysical Research Letters, 32, L01307, https://doi.org/10.1029/2004GL021661.

- Libowitzky, E. (1999) Correlation of O-H stretching frequencies and O-H···O hydrogen bond lengths in minerals. Monatshefte für Chemie/Chemical Monthly, 130, 1047–1059.
- Liu, L. (2002) Are hydrous phases more compressible? Implications for high-velocity zones in the deep mantle. Geophysical Journal International, 149, 37–43, https:// doi.org/10.1046/j.1365-246X.2002.01593.x.
- Liu, Z., Lager, G.A., Hemley, R.J., and Ross, N.L. (2003) Synchrotron infrared spectroscopy of OH-chondrodite and OH-clinohumite at high pressure. American Mineralogist, 88, 1412–1415, https://doi.org/10.2138/am-2003-1003.
- Liu, D., Smyth, J.R., Zhu, X., Miao, Y., Hu, Y., Chen, G., and Ye, Y. (2021) High-pressure vibrational spectra of humite-group minerals: Fluorine effect on thermodynamic properties and hydrogen bonds. Physics of the Earth and Planetary Interiors, 312, 106654, https://doi.org/10.1016/j.pepi.2021.106654.
- Lovett, R.A. (2014) Tiny diamond impurity reveals water riches of deep Earth. Nature, https://doi.org/10.1038/nature.2014.14862.
- Mao, H.K., Xu, J., and Bell, P.M. (1986) Calibration of the ruby pressure gauge to 800 kbar under quasi-hydrostatic conditions. Journal of Geophysical Research, 91 (B5), 4673, https://doi.org/10.1029/JB091iB05p04673.
- Mao, Z., Jacobsen, S.D., Jiang, F., Smyth, J.R., Holl, C.M., and Duffy, T.S. (2008) Elasticity of hydrous wadsleyite to 12 GPa: Implications for Earth's transition zone. Geophysical Research Letters, 35, L21305, https://doi.org/10.1029/2008GL035618.
- Mao, Z., Jacobsen, S.D., Jiang, F., Smyth, J.R., Holl, C.M., Frost, D.J., and Duffy, T.S. (2010) Velocity crossover between hydrous and anhydrous forsterite at high pressures. Earth and Planetary Science Letters, 293, 250–258, https://doi.org/10.1016/j.epsl.2010.02.025.
- Mao, Z., Lin, J.-F., Jacobsen, S.D., Duffy, T.S., Chang, Y.-Y., Smyth, J.R., Frost, D.J., Hauri, E.H., and Prakapenka, V.B. (2012) Sound velocities of hydrous ringwoodite to 16 GPa and 673 K. Earth and Planetary Science Letters, 331–332, 112–119, https://doi.org/10.1016/j.epsl.2012.03.001.
- Monkhorst, H.J. and Pack, J.D. (1976) Special points for Brillouin-zone integrations. Physical Review B, Solid State, 13, 5188–5192, https://doi.org/10.1103/PhysRevB.13.5188.
- Mookherjee, M., Speziale, S., Marquardt, H., Jahn, S., Wunder, B., Koch-Müller, M., and Liermann, H.-P. (2015) Equation of state and elasticity of the 3.65 Å phase: Implications for the X-discontinuity. American Mineralogist, 100, 2199–2208, https://doi.org/10.2138/am-2015-5312.
- Mookherjee, M., Panero, W.R., Wunder, B., and Jahn, S. (2019) Anomalous elastic behavior of phase egg, AlSiO₃(OH), at high pressures. American Mineralogist, 104, 130–139, https://doi.org/10.2138/am-2019-6694.
- Noguchi, N., Moriwaki, T., Ikemoto, Y., and Shinoda, K. (2012) OH group behavior and pressure-induced amorphization of antigorite examined under high pressure and temperature using synchrotron infrared spectroscopy. American Mineralogist, 97, 134–142, https://doi.org/10.2138/am.2012.3904.
- Panero, W.R. and Stixrude, L.P. (2004) Hydrogen incorporation in stishovite at high pressure and symmetric hydrogen bonding in δ -AlOOH. Earth and Planetary Science Letters, 221, 421–431, https://doi.org/10.1016/S0012-821X(04)00100-1.
- Parry, S.A., Pawley, A.R., Jones, R.L., and Clark, S.M. (2007) An infrared spectroscopic study of the OH stretching frequencies of talc and 10 Å phase to 10 GPa. American Mineralogist, 92, 525–531, https://doi.org/10.2138/am.2007.2211.
- Pawley, A.R., Clark, S.M., and Chinnery, N.J. (2002) Equation of state measurements of chlorite, pyrophyllite, and talc. American Mineralogist, 87, 1172–1182, https:// doi.org/10.2138/am-2002-8-916.
- Pawley, A.R., Chinnery, N.J., Clark, S.M., and Walter, M.J. (2011) Experimental study of the dehydration of 10 Å phase, with implications for its H₂O content and stability in subducted lithosphere. Contributions to Mineralogy and Petrology, 162, 1279–1289,https://doi.org/10.1007/s00410-011-0653-0.
- Pearson, D.G., Brenker, F.E., Nestola, F., McNeill, J., Nasdala, L., Hutchison, M.T., Matveev, S., Mather, K., Silversmit, G., Schmitz, S., and others. (2014) Hydrous mantle transition zone indicated by ringwoodite included within diamond. Nature, 507, 221–224, https://doi.org/10.1038/nature13080.
- Perdew, J.P. (1991) Generalized gradient approximations for exchange and correlation: A look backward and forward. Physica B, Condensed Matter, 172, 1–6, https://doi.org/ 10.1016/0921-4526(91)90409-8.
- Perdew, J.P. and Yue, W. (1986) Accurate and simple density functional for the electronic exchange energy: Generalized gradient approximation. Physical Review B: Condensed Matter, 33, 8800–8802, https://doi.org/10.1103/PhysRevB.33.8800.
- Perdew, J.P., Burke, K., and Ernzerhof, M. (1996) Generalized gradient approximation made simple. Physical Review Letters, 77, 3865–3868, https://doi.org/10.1103/ PhysRevLett.77.3865.
- Ross, N.L. and Crichton, W.A. (2001) Compression of synthetic hydroxylclinohumite [Mg₃Si₄O₁₆(OH)₂] and hydroxylchondrodite [Mg₂Si₂O₈(OH)₂]. American Mineralogist, 86, 990–996, https://doi.org/10.2138/am-2001-8-905.
- Sanchez-Valle, C., Sinogeikin, S.V., Smyth, J.R., and Bass, J.D. (2008) Sound velocities and elasticity of DHMS phase A to high pressure and implications for seismic velocities and anisotropy in subducted slabs. Physics of the Earth and Planetary Interiors, 170, 229–239, https://doi.org/10.1016/j.pepi.2008.07.015.
- Sano-Furukawa, A., Komatsu, K., Vanpeteghem, C.B., and Ohtani, E. (2008) Neutron diffraction study of δ-AlOOD at high pressure and its implication for symmetrization of the hydrogen bond. American Mineralogist, 93, 1558–1567, https://doi.org/ 10.2138/am.2008.2849.

- Scott, H.P., Liu, Z., Hemley, R.J., and Williams, Q. (2007) High-pressure infrared spectra of talc and lawsonite. American Mineralogist, 92, 1814–1820, https://doi.org/10.2138/am.2007.2430.
- Shieh, S.R., Mao, H., Konzett, J., and Hemley, R.J. (2000) In-situ high pressure X-ray diffraction of phase E to 15 GPa. American Mineralogist, 85, 765–769, https://doi.org/10.2138/am-2000-5-616.
- Shieh, S.R., Duffy, T.S., Liu, Z., and Ohtani, E. (2009) High-pressure infrared spectroscopy of the dense hydrous magnesium silicates phase D and phase E. Physics of the Earth and Planetary Interiors, 175, 106–114, https://doi.org/10.1016/j.pepi.2009.02.002.
- Syracuse, E.M., van Keken, P.E., and Abers, G.A. (2010) The global range of subduction zone thermal models. Physics of the Earth and Planetary Interiors, 183, 73–90, https://doi.org/10.1016/j.pepi.2010.02.004.
- Tange, Y., Kuwayama, Y., Irifune, T., Funakoshi, K., and Ohishi, Y. (2012) P-V-T equation of state of MgSiO₃ perovskite based on the MgO pressure scale: A comprehensive reference for mineralogy of the lower mantle. Journal of Geophysical Research. Solid Earth, 117, B06201.
- Togo, A. and Tanaka, I. (2015) First principles phonon calculations in materials science. Scripta Materialia, 108, 1–5, https://doi.org/10.1016/j.scriptamat.2015.07.021.
- Tschauner, O., Huang, S., Greenberg, E., Prakapenka, V.B., Ma, C., Rossman, G.R., Shen, A.H., Zhang, D., Newville, M., Lanzirotti, A., and others. (2018) Ice-VII inclusions in diamonds: Evidence for aqueous fluid in Earth's deep mantle. Science, 359, 1136–1139, https://doi.org/10.1126/science.aao3030.
- Tsuchiya, J. and Mookherjee, M. (2015) Crystal structure, equation of state, and elasticity of phase H (MgSiO₄H₂) at Earth's lower mantle pressures. Scientific Reports, 5, 15534, https://doi.org/10.1038/srep15534.
- Tsuchiya, J., Tsuchiya, T., Tsuneyuki, S., and Yamanaka, T. (2002) First principles calculation of a high-pressure hydrous phase, δ-AlOOH. Geophysical Research Letters, 29, 15-1-15-4.
- Tsuchiya, J., Tsuchiya, T., and Tsuneyuki, S. (2005) First-principles study of hydrogen bond symmetrization of phase D under high pressure. American Mineralogist, 90, 44–49, https://doi.org/10.2138/am.2005.1628.
- Welch, M.D. and Wunder, B. (2012) A single-crystal X-ray diffraction study of the 3.65 Å-phase MgSi(OH)₆, a high-pressure hydroxide perovskite. Physics and Chemistry of Minerals, 39, 693–697, https://doi.org/10.1007/s00269-012-0523-y.

- Wirth, R., Vollmer, C., Brenker, F., Matsyuk, S., and Kaminsky, F. (2007) Inclusions of nanocrystalline hydrous aluminium silicate "Phase Egg" in superdeep diamonds from Juina (Mato Grosso State, Brazil). Earth and Planetary Science Letters, 259, 384–399, https://doi.org/10.1016/j.epsl.2007.04.041.
- Wunder, B., Wirth, R., and Koch-Muller, M. (2011) The 3.65 Å phase in the system MgO-SiO₂-H₂O: Synthesis, composition, and structure. American Mineralogist, 96, 1207–1214, https://doi.org/10.2138/am.2011.3782.
- Wunder, B., Jahn, S., Koch-Müller, M., and Speziale, S. (2012) The 3.65 Å phase, MgSi(OH)₆: Structural insights from DFT-calculations and T-dependent IR spectroscopy. American Mineralogist, 97, 1043–1048, https://doi.org/10.2138/ am.2012.4022.
- Yagi, T., Mao, H.-K., and Bell, P.M. (1978) Structure and crystal chemistry of perovskite-type MgSiO₃. Physics and Chemistry of Minerals, 3, 97–110, https:// doi.org/10.1007/BF00308114.
- Yang, H., Hazen, R.M., Prewitt, C.T., Finger, L.W., Ren, L., and Hemley, R.J. (1998) High-pressure single-crystal X-ray diffraction and infrared spectroscopic studies of the C2/m-P2₁/m phase transition in cummingtonite. American Mineralogist, 83, 288–299, https://doi.org/10.2138/am-1998-3-412.

Manuscript received March 4, 2022
Manuscript accepted September 16, 2022
Accepted manuscript online September 29, 2022
Manuscript handled by Susannah Dorfman

Endnote:

¹Deposit item AM-23-88515, Online Materials. Deposit items are free to all readers and found on the MSA website, via the specific issue's Table of Contents (go to http://www.minsocam.org/MSA/AmMin/TOC/2023/Aug2023_data/Aug2023_data.html).